Analysis and Design of Key Phenomena in Electronics: Nanostructures and Devices

Neil Goldsman and Akin Akturk

Electrical and Computer Engineering, University of Maryland, College Park, MD 20742

ABSTRACT

We have developed techniques to model electron dynamics in carbon nanotubes and hypothetical field effect devices that incorporate nanotubes into their structure. We use both Monte Carlo methods that are based on semiclassical transport, and distributed analyses that utilize quantum corrected semiconductor equations. The MC calculations predict velocity oscillations that are spatially distributed along the carbon nanotube. A quantum corrected semiconductor mathematical model is presented for CNT-MOSFET device simulation. Calculations predict improved performance of CNT-MOSFETs over conventional structures under certain conditions.

1. INTRODUCTION

In this paper we describe physical electronic properties of carbon nanotubes (CNTs), and CNT embedded MOSFETs. We focus on electron transport characteristics. We start with a single nanotube, where electron dynamics are modeled in detail. Using information from detailed CNT simulation, we then develop reduced models to predict how MOSFET would operate if CNTs were to be embedded in the channel.

2. CARBON NANOTUBE MODELING

We report Monte Carlo (MC) simulation results that show position-dependent velocity oscillations and length effects in semiconducting single-walled zig-zag carbon nanotubes, as shown in Fig. 1. The simulations show velocity oscillations at Terahertz frequencies, which approach phonon frequencies, and velocity values reaching 7×10^7 cm/s. Also, our investigations on length effects show that average velocity first overshoots, then rolls off as the tube length increases, and finally reaches its steady state value. In addition, we include quantum effects due to finite lengths of the tubes, as well as their circumference.
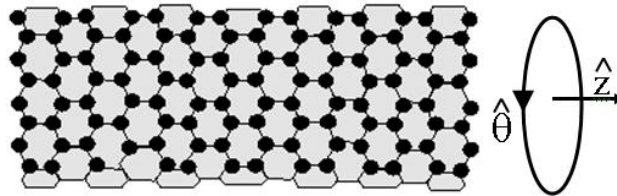

Fig. 1: A single wall zig-zag carbon nanotube, with fundamental indices n and $m = 0$, and length L [1].

Recently, carbon nanotubes have prompted interest as potential candidates for use in nanoscale electronics [2,3]. This is due to their favorable structural and, especially, electrical characteristics such as high electron velocities approaching 1×10^8 cm/s at high fields and 1×10^7 cm/s at low fields, resulting in low-field electron mobilities as much as ten times higher than that of Si. Additionally, they exhibit negative differential velocities (NDV), similar in that respect to GaAs, opening possibilities for their use in oscillators and, therefore, communication networks. When used in circuits, our simulations indicate that they may oscillate at very high frequencies in the terahertz range, enabling data rates approaching terabits per second. Thus, to fully investigate potential gains due to CNT usage in nanoelectronics, we developed an MC CNT simulator to extract pertinent electrical CNT parameters.

CNTs are hollow tubes rolled up from planar graphite sheets (graphene). Single-walled CNTs have nanometer-scale diameters ranging from several to a few hundred angstroms. A CNT can be uniquely identified by its fundamental

indices *n* and *m*, which are the coefficients of the unit vectors of the hexagonal graphite lattice used to specify the wrapping angle and the diameter. We can also relate the electrical properties of a CNT to its fundamental indices *n* and *m* such that they are metallic if *n−m* is a multiple of three, or else, semiconducting with a bandgap inversely proportional to $\sqrt{n^2 + m^2 + nm}$ [4,5]. (Here, *n* does not refer to electron concentration unless stated otherwise.)

Here, we concentrate on the most studied single-walled semiconducting CNT topology, which is the zig-zag (*n,m* = 0). From now on, "CNT" means semiconducting single-walled zig-zag carbon nanotubes. We have developed a Monte Carlo simulator for CNTs, and have used it to investigate average electron velocity as a function of position. We have also calculated average electron velocity as a function of tube length, for tubes of various indices. Next, using average velocity versus applied field curves, we have derived mobility models to be used in device simulators. To fully characterize the CNTs in our device simulators, we have also extracted additional CNT electrical parameters such as intrinsic carrier concentration and electron affinity. We first briefly describe our Monte Carlo simulator, and then show our calculated results, which are in agreement with theoretical [4,5] and experimental [6,7] data.

2.1. Energy Spectra

We first employ a Monte Carlo (MC) simulator [4,5] to characterize fundamental transport properties of CNTs. Then, we incorporate these properties into our device simulators. These properties include electron drift velocity versus electric field curves, as well as CNT mobilities for zig-zag single wall CNTs. (The zig-zag CNT is probably the most studied semiconducting nanotube topology. Semiconducting zig-zag CNTs have fundamental indices (*n*,0), where *n* takes on integer values other than multiples of three.) To obtain these properties, we begin with the physical CNT system, where electrons are confined around the circumference, and move relatively freely along the tube in the direction of the longitudinal axis. Therefore, one can write the appropriate plane wave solutions that satisfy periodic boundary conditions, distinguished by the quantum number *β*, for the given CNT circumference. However, along the tube, electrons are not confined for long tubes. Thus, the wavevector can be written as follows:

$$\vec{k} = k_z \hat{z} + \frac{2\beta}{d} \hat{\theta} .$$

(1)

Here $\hat{z}$ is parallel to the tube axis, and $\hat{\theta}$ is the unit vector along the circumference. Discrete values around the circumference, *β*, are bounded by the fundamental tube index $\pm n$, to take advantage of the symmetry lines in the CNT Brillouin zone.

In the simulator, electrons drift due to an external field along the length of the tube in real space, and in one of the first three lowest CNT energy subbands in the energy-momentum space until they probabilistically scatter with acoustic or optical phonons. They then start traveling again on the tube with their new energy and momentum that are calculated using the energy and momentum conservation laws. This process is repeated until the electron exits the tube from one end. Here, we consider scattering by optical and acoustic phonons, causing inter and intra subband, and inter-valley and intra-valley transitions. Both scattering mechanisms are treated within the deformation potential method using the Fermi's Golden Rule.

2.1.1. Monte Carlo for Long Tubes

Due to confinement around the circumference, the bandstructure splits into a system of subbands when graphene is wrapped into a CNT [1]. Each of the subbands has a characteristic effective mass, mobility and band energy minima. We determine the energy levels of CNTs by applying zone-folding methods to graphene [8]. From the two-dimensional graphene band diagram, we cut one-dimensional slices, whose numbers and locations are set by the fundamental tube indices (*n*,0). The resulting CNT (*n*,0) energy dispersion relation, which is determined by applying zone-folding methods to the graphene energy dispersion relation that is calculated using the tight binding model [8], is shown below (Here *E* is used for the energy, and *F* is used for the field):

$$E(k_z, \beta) = \pm\gamma\sqrt{1 + 4\cos\left(\frac{Tk_z}{2}\right)\cos\left(\frac{\pi\beta}{n}\right) + 4\cos^2\left(\frac{\pi\beta}{n}\right)} \qquad \text{(eV)} \qquad (2)$$

Here, T is the length of the translational vector, which is equal to 4.26Å for the zig-zag tubes. Also, we use 3eV for the nearest-neighbor π-hopping integral γ [4,5]. Now, we determine the lowest three subbands, using the above expression. We first take the derivative of Eqn. 2 with respect to k_z, or k ($=k_z$).

$$\left|\frac{dE}{dk}\right| = 9\left|\frac{T\sin\left(\frac{Tk}{2}\right)\cos\left(\frac{\pi\beta}{n}\right)}{E}\right| \qquad (3)$$

For the k values that give subband minima, the derivative of Eqn. 2 is zero. Since sine is zero when k is zero, we have an energy minimum of each subband at $k = 0$. Moreover, we also need to check the boundaries. However, in this case, energy values at the boundaries ($\pm\pi/T$) are higher than energy values at $k = 0$.

Next, we determine wavevector indices, β, for the lowest three subbands by searching for the integers from zero to n that give the lowest three values for E(0, β). To shorten our search time, we take the derivative of Eqn. 2 with respect to β at $k = 0$.

$$\left|\frac{dE}{d\beta}\right|_{k=0} = 6\frac{\pi}{n}\left|\sin\left(\frac{\pi\beta}{n}\right)\left(1 + 2\cos\left(\frac{\pi\beta}{n}\right)\right)\right| \qquad (4)$$

The above derivative tells us that the lower subbands are either around $\beta = 0$ or $\beta = 2n/3$. Using the cosine term, we can show that they are around $\beta = 2n/3$. Since β takes on integer values, β for the lowest subband is $2n/3$ rounded to the nearest integer. Furthermore, we can also find the β values using the Brillouin zone. More specifically, from geometrical considerations in the Brillouin zone, we also found β, for the lowest subband, equal to $2n/3$ rounded to the nearest integer [4,5]. Additionally, since cosine is an even function, $-\beta$ and β give the same energy. Therefore, we here have two identical valleys with each having three subbands.

2.1.2. Incorporating Quantization Effects due to CNT Length

We consider effects due to finite length of the tubes, which lead to discretization in energy dispersion curves [1]. For a zig-zag tube, the length of the translational vector is roughly 4.26Å; therefore, maximum electron momentum, which is equal to pi (π) over this value, is approximately 0.74 Å^{-1}. Furthermore, minimum momentum step is related to the length of the tube, which is $2\pi/L$. Also, for the longest tube we simulate, which is 100nm long, we have about twenty times more steps. Using this information, we include the finite contribution of longitudinal quantization on electron transport during our simulations. We calculate scattering rates using the continuous band. We have modified our MC simulator to account for this quantization. In our modified MC, the electron drifts along the tube until it hits an energy step that needs to be overcome to achieve higher momentum values (This is true only for positive momentum values). At this point, we determine reflection and transmission probabilities for this barrier. We below show the backward (reflection) scattering rate for an electron with a momentum k at the edge of a step, which is $2\pi/L$ ($= \Delta k$) wide.

$$\Gamma_{ref} = \left(\frac{\Delta k}{2k}\right)^2 \qquad (5)$$

When an electron, with momentum k_1 and energy $E(k_1)$, hits an energy barrier ΔE, upon successful transmission, it has a new momentum k_2 that satisfies the energy conservation. For such a system, the transmitted and reflected power ratios are:

$$R = \left(\frac{k_2 - k_1}{k_2 + k_1} \right)^2 \qquad (6)$$

$$T = 1 - R \qquad (7)$$

In our case, $k_2 - k_1$ is $2\pi/L$. Since the electron keeps gaining energy due to the applied field according to the continuum model, to retain consistency, it does not suddenly gain energy if transmitted. Therefore, $k_2 + k_1$ becomes $2k_1$. Depending on the likelihood of transmission, the electron either continues gaining momentum until it hits the next step or reflects back to negative momentum values ($-k_1$). The longer the CNT ($\Delta k \rightarrow 0$), the smaller the barriers become, with reflection coefficients approaching zero and the continuum approximation for long tubes.
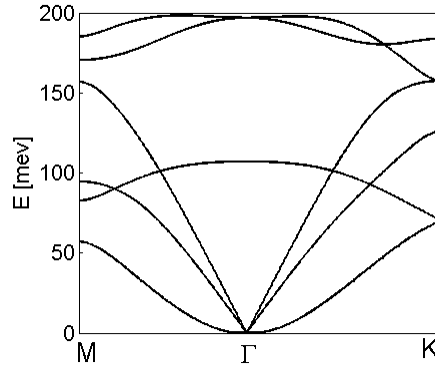

Fig. 2: The graphene phonon dispersion curves along the symmetry lines.

2.1.3. Phonon Energy Dispersion Relations

To obtain CNT phonon energy spectra, we start from the phonon dispersion curves of the graphene. We first calculate the graphene phonon spectra using the forth nearest neighbor force constant model, where force − equivalently, spring − constants determine the inter-atomic interactions. We derive this model from the equation of motion, as follows [8].

$$M_i \frac{\partial^2 u_i}{\partial t^2} = \sum_j K_{ij} \left(u_j - u_i \right) \qquad (8)$$

Above, i and j represent one of the N atoms in the unit cell. In addition, M_i and u_i are the mass and the location of the ith atom, and the force constant between the ith and the jth atoms is K_{ij}.

To obtain phonon spectra, we first apply Fourier transform. Canceling out common terms, and using the orthogonality condition, we get a matrix equation of the form $\overline{\overline{A}}\,\overline{u}_k = 0$, where $\overline{u}_k = [u_{k_1} ... u_{k_i} ... u_{k_N}]^T$. The diagonal elements of $\overline{\overline{A}}$ are $\left(\sum_j K_{ij} - M_i \omega^2 \right) - K_{ii} e^{i\vec{k}.\left(\vec{r}_i - \vec{r}_i\right)}$. Additionally, the off-diagonal elements of $\overline{\overline{A}}$ are $-K_{ij} e^{i\vec{k}.\left(\vec{r}_i - \vec{r}_j\right)}$. Furthermore, for different k values, we find the corresponding eigenvalues of $\overline{\overline{A}}$. Tracing over all ks gives the dispersion curve of the material.

We next show our calculated phonon dispersion curves in Fig. 2, using the prescription described before. We take the mass of a carbon atom in the graphene as about $12m_o$, where m_o is the free electron mass. Additionally, bond lengths are 2.49Å. Furthermore, to find the dispersion curves of the CNT, we approximate the dispersion curves of graphene around the Γ and K points, which are important for transport. We then calculate the phonon energy spectra by applying zone-folding methods to graphene. Our calculated energy dispersion relations for acoustic and optical phonons can be found in [5]. We give a generalized formula for our dispersion curves below:

$$E_p(q, \eta) = E_{p0}(\eta) + \hbar v_s \theta\left(|q| - \lambda \left|\frac{\eta}{d}\right|\right) \qquad (9)$$

Here q, η, θ and λ are respectively the phonon wavevector along the length of the tube, phonon wavevector index around the circumference of the tube, a dispersion coefficient and a kink factor that is zero for optical phonons and one for acoustic phonons. Additionally, d is the diameter of the tube, and v_s is the longitudinal sound velocity in graphene, which is 200 Å /ps.

2.2. Electron-Phonon Scattering Rates

To determine the electron-phonon scattering rates, we employ the deformation potential approximation and Fermi's Golden Rule [1,4,5]. In this scheme, the total scattering rate ($\Gamma_i(k)$) for an electron in subband i with a wavevector k (and β_i) to any other subband j by absorbing or emitting an intra-valley ($q, \eta = \beta_i - \beta_i$) or inter-valley ($q, \eta = \beta_i - \beta_i \pm (2n)$) phonon can be written as follows:

$$\Gamma_i(k) = \sum_q \frac{\hbar D^2 Q^2 DOS_j(E(k+q))}{2\rho E_p(q, \eta)} \left[N(q, \eta) \pm \frac{1}{2}\right] \qquad (10)$$

Here, D is the deformation potential taken to be 9eV, Q is a coefficient for optical and acoustic phonons, DOS is the density of states calculated by the inverse slope of Eqn. 2, ρ is the linear mass density, and N is the Bose-Einstein phonon occupation number at equilibrium. Additionally, the above sum has non-vanishing values for phonon wavevectors that satisfy energy and momentum conservation laws:

$$E(k+q, \beta_j) - E(k, \beta_i) - E_p(q, \beta_i - \beta_j \pm (2n)) = 0 . \qquad (11)$$

We below show the density of states. It has singularities near the band minima, where k and $\sin(k)$ are zero. To avoid numerical problems, we add an epsilon to k when it is exactly zero. For proper handling of this, we need to use the collision broadening concept. However, our investigations show that they give similar results for this problem, enabling us to use the aforementioned truncation for fast computation.

$$DOS_j(E(k)) = \left|\frac{E(k)}{9T \sin\left(\frac{Tk}{2}\right) \cos\left(\frac{\pi \beta_j}{n}\right)}\right| \qquad (12)$$

In addition, the zig-zag CNTs have a number $2n$ of hexagons in their unit cells, with each hexagon weighing M ($12m_o$). Therefore, the linear mass density is $2nM$ over AT, where T is the length of the translational vector, and A is the Avogadro's number.
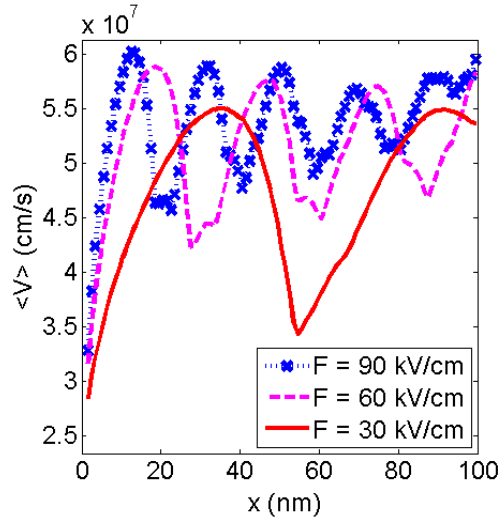
Fig. 3: Average local electron velocities on 100nm-long *n* =13 CNT [1].

2.3. Velocity Curves

2.3.1. Position-Dependent Velocity

Using our Monte Carlo simulator, we first investigate how local CNT electron velocities change by varying the applied field [1]. To obtain average local electron velocities as a function of position, we inject electrons, which are picked from a Fermi-Dirac distribution, from both ends of the tube. We then keep track of their position, average energy and momentum. Our calculated average electron velocities on a 100nm-long CNT with the fundamental index of 13 (diameter, *d*= 1nm) is shown in Fig. 3. From ΔE over $\hbar \Delta k$, which is also equal to *l* over τ, we calculate average velocities. The newly introduced variables ΔE, Δk, *l* and τ are change in total energy, change in total momentum, length and time spent around the vicinity of a given location, respectively. The two aforementioned methods to calculate average velocities give the same answer because of the following reasons. The $\hbar \Delta k$ term is equal to change in momentum Δp, which is also equal to the product of the elapsed time Δt (= τ) and the electric force (*qF*) due to the applied field *F*. In addition, change in energy due to drift can be calculated from force, due to the electric field, (*qF*) times distance *l*. Therefore, $\Delta E / \hbar \Delta k = = qFl / qF\tau$, resulting in l / τ that was shown before.

Simulations predict velocity oscillations at Terahertz frequencies, with a highest frequency of approximately 30THz among the simulated cases. From the velocity versus location curve of the *n*=13 tube under 100kV/cm, shown in Fig. 3, we take the average wavelength and velocity of the oscillations roughly as 17nm and 5×10^7cm/s. This results in f, which is 5×10^7cm/s over 17×10^{-7}cm = 30THz. (Here, we have velocity oscillations in space, which might induce dipole formations within the material. These dipoles are likely to travel on the CNT, resulting in velocity oscillations in time. To observe if this phenomenon does indeed occur, transient simulations need to be performed.)

We associate such high oscillation frequencies with the phonon spectrum and the one-dimensional nature of the system, which result in the average scattering rates and momenta. More specifically, the average scattering rate has oscillations with a period of 16nm (first maximum) and 20nm (second maximum) for the first few cycles and at their harmonics thereafter. Under an applied field of 100kV/cm, an electron will gain 160meV and 200meV after a free flight of 16nm and 20nm, respectively. These 160meV and 200meV energies above the energy band minima correspond to energy differences sufficient enough to have inter-valley acoustic and optical, and intra-valley and inter-valley optical phonon emissions in addition to all the other scattering mechanisms. When this happens, electrons are much more likely to scatter to lower momentum values where densities of states (equivalently scattering rates to those states in our one dimensional system) are much higher. In addition, we observe that all except a negligible portion of the electrons travel

in the first subband, thus eliminating the possibility to have the velocity oscillations due to transfer of electrons from the first to the second subband, and vice versa.

In summary, we theoretically show that one-dimensional CNT system has velocity oscillations with Terahertz frequencies, approaching to those of phonons. This may facilitate very high frequency oscillators similar to Gunn diodes, opening new paradigms for Terahertz RF electronics.

3. CARBON NANOTUBE EMBEDDED MOSFET MODELING

As we approach the end of the semiconductor roadmap, investigators are exploring new paradigms for electronic devices. Carbon nanotubes (CNTs) are being explored as a structure that may play a leading role in future electronic systems [2,3,9]. CNTs are planar graphite sheets (graphene) that are seamlessly wrapped into tubes. CNTs possess favorable electrical characteristics, and can be fabricated in dimensions as small as 8Å in diameter. The electrical characteristics of CNTs vary with the diameter and the wrapping angle of the graphene [8]. Both the diameter and the wrapping angle can be described by the tube's fundamental indices (l,m) (Standard notation uses (n,m); however, l is used hereafter instead of n to avoid confusion with electron concentration). Theory indicates that CNTs can be metallic or semiconducting depending on the fundamental tube indices (l,m), with bandgap of the semiconducting tube inversely proportional to the CNT diameter. Experimental and theoretical analyses show semiconducting CNTs having electron mobilities even higher than $10^5 cm^2/Vs$, with peak drift electron velocities that can be as much as five times higher than that of silicon [4-7,10]. Experiments also have demonstrated the viability of CNT-based FETs [2,11], and CNT-SOI type MOSFETs [12,13]. Furthermore, preliminary research has been done to model and design CNT embedded bulk MOSFETs [3,14].
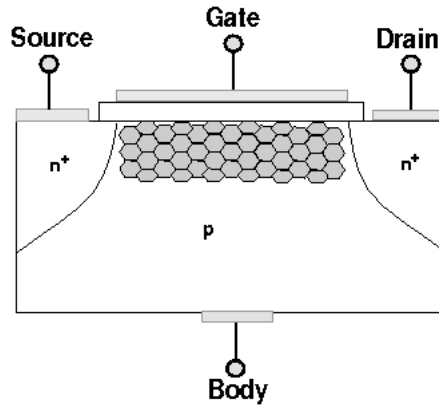

Fig. 4: CNT embedded MOSFET device [3].

Here, we investigate several hypothetical CNT-MOSFET devices, similar to the one shown in Fig. 4. Our calculations indicate that if successfully fabricated, CNT-MOSFETs can have improved device performance over conventional MOSFETs [3,14]. To investigate the potential attributes of the new design, we developed a methodology for modeling nanoscale CNT-MOSFETs. It includes determination of the electrical characteristics of single wall zig-zag CNTs, and the merging of the CNT results into our quantum device solver. To electrically characterize the CNT, we developed a Monte Carlo (MC) simulator for CNTs, as described previously. Using the MC results, we derive analytical models for CNT parameters such as mobility and density of states. Once we obtain CNT parameters, we import them to our quantum device solver. Our device solver is based on the semiconductor equations, modified to account for the CNT-silicon (CNT-Si) barrier [3] and quantum effects. We solve these coupled equations on a mesh within our CNT-MOSFET device. The solution gives results, which include CNT-MOSFET current voltage curves, and the electron concentration profile in both the bulk MOSFET and the CNT enhanced channel. In addition, we also do similar analyses for CNT embedded SOI-MOSFETs.

Next, we show the methodology developed to obtain device performance details of CNT-MOSFETs. We first show our algorithm to resolve the quantum and the CNT-Si barrier effects. After we give an insight to our CNT-Si device simulator, we present our calculated results for the CNT-MOSFETs.

3.1. Quantum CNT-MOSFET Modeling

We propose a novel MOSFET design that embodies single wall zig-zag semiconducting Carbon Nanotubes (CNTs) in the channel. Investigations show that CNTs have high low-field mobilities, which can be as great as $4 \times 10^4 \mathrm{cm}^2/\mathrm{Vs}$. Thus, we expect that MOSFET performance can be improved by embedding CNTs in the channel. To investigate the performance of a newly proposed CNT-MOSFET device, we develop a methodology that connects CNT modeling to MOSFET simulations. Our calculations indicate that by forming high mobility regions in the channel, MOSFET performance can be boosted. However, barriers formed between the CNT and the Si due to the variations of the bandgaps and the electron affinities can degrade MOSFET performance improvements. Our calculations were obtained by building on our existing CNT Monte Carlo (MC) simulator [4,5] and quantum based device solver [3,14].

3.1.1. Quantum CNT-Silicon MOSFET Simulator

We develop a two-dimensional quantum device solver based on the Poisson equation and the modified semiconductor equations. We here take the invariance in the width direction as retained by the introduction of tubes in the channel. Since CNTs in our simulations have small diameters, the bending of the field around the tube is limited to ensure smooth field curves. The governing equations are listed below in the order of Poisson, quantum/CNT-Si electron current continuity, and quantum/CNT-Si hole current continuity equations.

$$\nabla^2 \phi = -\frac{q}{\varepsilon}\left(p - n + D\right) \tag{13}$$

$$\frac{\partial n}{\partial t} = \frac{1}{q}\nabla.J_n + GR_n \tag{14}$$

$$\frac{\partial p}{\partial t} = -\frac{1}{q}\nabla.J_p + GR_p \tag{15}$$

Here, the variables $n(p)$, J_n (J_p), D and GR_n (GR_p) are electrostatic potential, electron (hole) concentrations, electron (hole) current densities, net dopant concentration, and electron (hole) Shockley-Hall-Read net generation-recombination rates, respectively. We next define electron and hole current densities J_n and J_p as follows:

$$J_n = -qn\mu_n\nabla\left(\phi + \phi_{QM} + \phi_{HS}^n\right) + \mu_n kT\nabla n \tag{16}$$

$$J_p = -qp\mu_p\nabla\left(\phi - \phi_{QM} - \phi_{HS}^p\right) - \mu_p kT\nabla p \tag{17}$$

We here symbolize electron-hole mobilities by μ_{n-p}. We also introduce two additional effective potential terms ϕ_{QM} and ϕ_{HS} to account for the quantum and the CNT-Si barrier effects, respectively. We next will discuss how these two phenomena are taken care of by the effective potential terms starting from the CNT-Si barrier effects.

Solution of the CNT-MOSFET system requires proper handling of two phenomena. The first is the effect of the quantum well formed at the Si-SiO$_2$ interface that causes band splitting, thus lowering of the carrier concentration. Second one is the influence of the barrier formed at the CNT-Si interface that results from the different bandstructures

and electron affinities of the CNT and silicon. A quantum well may also form at the CNT-Si junction due to the band-offsets.

We resolve the effects of CNT-Si barrier through the use of revised current equations with the following effective potential terms:

$$\phi_{HS}^{n} = \frac{1}{q}\left(\chi - \chi^{Si}\right) + \frac{kT}{q}\ln\left(\frac{n_o}{n_o^{Si}}\right) \tag{18}$$

$$\phi_{HS}^{p} = -\frac{1}{q}\left(\chi + E_G - \chi^{Si} - E_G^{Si}\right) - \frac{kT}{q}\ln\left(\frac{n_o}{n_o^{Si}}\right) \tag{19}$$

$$\phi_{QM} = \frac{2\hbar^2}{12q\sqrt{n}}\left[\frac{1}{m_{\Box}}\frac{\partial^2\sqrt{n}}{\partial x^2} + \frac{1}{m_{\perp}}\frac{\partial^2\sqrt{n}}{\partial y^2}\right] \tag{20}$$

Here, n_o is the intrinsic carrier concentration at a grid point on our device, and n_o^{Si} is the intrinsic carrier concentration of silicon. We note that n_o takes on either the intrinsic carrier concentration of the CNT or the Si, depending on the location within the CNT-MOSFET. Also, χ is the electron affinity at a grid point on our device and is either equal to χ_{Si} or χ_{CNT}. We subtract χ_{Si} from χ_{CNT}, because our reference material is the Si. In addition, E_G, like χ and n_o, refers to the same material in space. It takes on the bandgap value of either the CNT or the Si depending on the location inside our CNT-MOSFET. Furthermore, in Eqn. 20, x is parallel to the MOSFET channel and tube axis, and y is normal to x. Also, we use the effective mass of the Si or the CNT depending on the direction and location.

Using a combination of numerical methods, we finally solve our coupled quantum semiconductor Eqns. 13-15 along with Eqns. 16-20, for the electrostatic potential, quantum/CNT-Si electron concentration, and quantum/CNT-Si hole concentration for the CNT-MOSFET. More specifically, at each grid point on our mesh, we first calculate values for the effective heterostructure potentials for the electrons and holes. We then add these effective potentials to the electrostatic potentials ($\theta_{i,j}$) at each grid point; i, j. Next, we use these newly calculated potentials in the Bernoulli functions of the Scharfetter-Gummel discretization scheme. We apply the same method of calculating potentials to find the electron and hole concentrations to be used in the discretized Poisson equation. Since we take the reference as the Si, we use intrinsic carrier concentration n_o of the Si in the semiconductor equations wherever an intrinsic carrier concentration is needed, except for the calculation of the aforementioned heterostructure effective potentials. Next, we solve for the electrostatic potential, and the electron and hole concentrations. To solve for the state variables, we first use the Gauss-Seidel method, and then simultaneously find corrections to all the state variables using the Newton-Raphson method. We obtain the classical solution once the corrections are insignificantly small. At this point, we calculate the quantum effective potentials at each point in the channel of our device. We then add these quantum effective potentials to the electrostatic potentials and the heterostructure effective potentials, and then use the new potential terms to calculate the drift components of carrier's current densities. As before, we first use the Gauss-Seidel method to get an estimate for the solution. For the final tune-up, we use a matrix solver to calculate corrections for the state variables using the Newton-Raphson method. Once the aforementioned variables are determined, we use them to calculate the current-voltage characteristics of the CNT-MOSFET.

3.1.2. Simulation Results

We applied our modeling methodology to simulate a 0.15μm well-tempered (having high on/off current ratio) CNT-MOSFET. We first simulated CNT-MOSFETs with a single layer of CNT in the MOSFET channel parallel to the interface as illustrated in Fig. 4. The parameter we investigate in these simulations is the effect of different diameter tubes. We next study how incorporating additional layers of 8Å -diameter tubes affects the device characteristics.
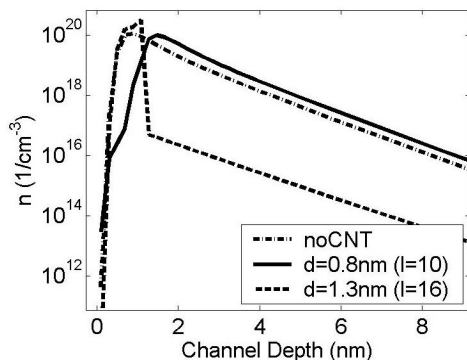
Fig. 5: Calculated electron concentration profile in the middle of the CNT-MOSFET channel for different diameter CNTs (V_G=1.5V, V_D and V_S are 0V), starting from the Si-SiO$_2$ interface and going down about 9nm [3].

In Fig. 5, we show our calculated electron concentration in the vertical direction of the MOSFET channel, starting from the Si-SiO$_2$ interface. We applied 1.5V to the gate terminal, and grounded others. CNT-MOSFET contains one layer of tube. The device with the medium diameter tubes (d =13Å) shows high concentrations in the channel. The abrupt change in the carrier concentration can be attributed to the differences in the conduction band offset between the CNT and the Si. We associate this with the high intrinsic carrier concentration and lower work function (compared to the Si) of the larger diameter tubes, which attract electrons even in the absence of a gate field. On the other hand, the intrinsic carrier concentration of the d =8Å CNT is close to that of the Si, and the CNT has a higher work function. Thus a potential well is formed on the tube which in turn pushes electrons away from the channel of this CNT-MOSFET. Thus, the larger diameter CNTs appear to be likely to sustain large transconductances.
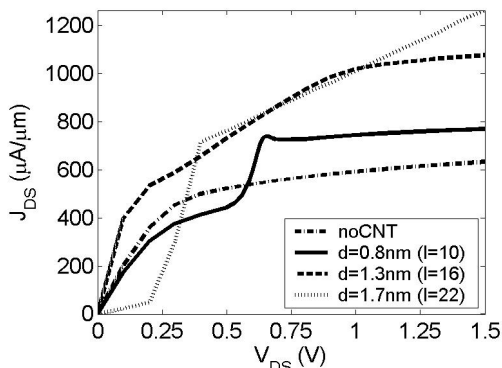

Fig. 6: Current-voltage curves for CNT-MOSFETs with different diameter CNTs. V_{GS}=1.5V [3].

We next investigate whether the band-offsets between the wider tubes and silicon appear to negate the potential improvement of higher electron concentration in the channel of the larger diameter tube CNT-MOSFETs. Therefore, we obtain the current-voltage characteristics of the 0.15μm CNT-MOSFETs in the subthreshold, linear and saturation regions. In Fig. 6, we compare the drain current density versus applied drain voltage curves for four MOSFET configurations. One set of curves is for the conventional MOSFET without any CNTs in the channel. The other three sets of curves are for the single layer CNT-MOSFETs with small (8Å), medium (13Å) and large (17Å) diameter CNTs in the channel, just below the SiO$_2$. We find that for high bias conditions, CNT-MOSFETs utilizing larger diameter tubes attain higher drive currents than the ones having the small diameter tubes, followed by the conventional MOSFET.

One of the main differences in performance between CNT-MOSFETs can be attributed to the height of the barrier formed at the CNT-Si junction. The smaller diameter tubes have less barrier height offset since their intrinsic carrier concentration is closer to that of the silicon. However, the small diameter tubes form a potential well at the channel, unlike the larger diameter tubes that attract more electrons as the diameter gets bigger. The CNT-MOSFETs have

improved drive current characteristics over the conventional MOSFET. We attribute these higher currents to larger channel electron concentrations, as shown in Fig. 5, and larger mobility values in the CNTs. However, the large diameter tube CNT-MOSFET behaves more like a resistor with a low output resistance due to its band-offset and high mobility. In addition, the small diameter tube CNT-MOSFET has a jump in its current drive around V_{DS}=0.6V, where the electron concentration on the tube suddenly jumps from the levels shown in Fig. 5 (10^{16}cm^{-3}) to higher values (10^{18}cm^{-3}) indicating that new subbands are populated on the tube as we increase the drain bias.

The small diameter tube CNT-MOSFET has a steep subthreshold slope (like the conventional device) with a lower leakage level and higher drive current when compared to the conventional device at high gate biases. We attribute this to the band-offset and high mobility associated with the small diameter CNTs. Additionally, the small diameter CNT-MOSFET shows negative differential transconductance. We associate this with the occupation of new subbands on the tube as the gate bias increases. For the same bias range, larger diameter tube CNT-MOSFETs have a much higher leakage level which gets worse as the drain bias increases. However the on/off current ratio is still on the order of a thousand, which should enable their use as FETs but may limit their low power applications. We attribute this to the band-offsets and high mobility of the larger diameter tubes.

We next investigate ways to increase the electron concentration in the channel of the small diameter tube CNT-MOSFET to achieve even higher current drives. The small diameter tube device already has improved subthreshold characteristics, which are mainly controlled by the band-offsets at the drain and source sides. However, drive current is controlled by the gate via the electron channel formed in the CNT-MOSFET. Since electron concentration is low on the tube due to confinement, we add extra layers of CNTs in the vertical channel direction to increase the physical size of the well. (The length of the tube is still in the direction of the channel.) Therefore, more electrons can fit in the well. Furthermore, we show the current curves for high gate bias in Fig. 7, where the highest current is supplied by the three layered CNT-MOSFET. Additionally, the jump in the current drive of the one layered device becomes less pronounced as the number of layers increases. We associate this with less confinement in a well with bigger dimensions, where most of the states are already occupied.
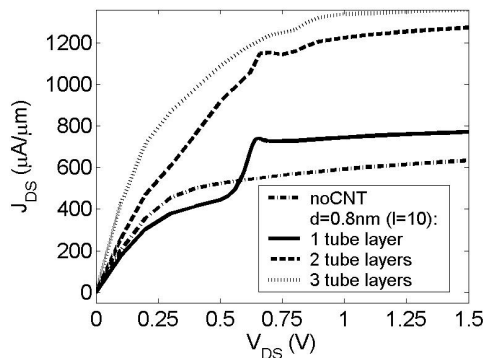

Fig. 7: Current-voltage curves for CNT-MOSFETs with CNTs of 0.8nm in diameter and varying number of tube layers (planar CNT sheets) in the vertical channel direction. V_{GS}=1.5V [3].

4. CONCLUSION

New modeling techniques have been developed to analyze electron transport in semiconductor CNTs, and related devices. These techniques predict interesting electrical phenomena. Monte Carlo simulations of individual CNTs predict extremely high electron low field mobility. At high fields, MC modeling predicts velocity oscillations in space and negative differential mobility. This may lead to applications in THz wireless communication electronics. We also propose new designs for field effect transistors which have CNTs embedded in the channel. The CNT-FETs exhibit improved transconductance over conventional devices under certain conditions of operation.

5. References

1. A. Akturk, G. Pennington, N. Goldsman, and A. Wickenden, "Quantum electron transport in carbon nanotubes: velocity oscillations and length dependence," *Proceeding of SISPAD*, 31 (2006).
2. A. Bachtold, P. Hadley, T. Nakanishi, and C. Dekker, "Logic circuits with carbon nanotube transistors," *Science* 294, 1317 (2001).
3. A. Akturk, G. Pennington, and N. Goldsman, "Quantum modeling and proposed designs of cnt-embedded nanoscale mosfets," *IEEE Trans. Electron Dev.* 52(4), 577 (2005).
4. G. Pennington, and N. Goldsman, "Semiclassical transport and phonon scattering on electrons in semiconducting carbon nanotubes," *Phys. Rev. B* 68, 45426 (2003).
5. G. Pennington, and N. Goldsman, "Monte carlo study of electron transport in a carbon nanotube," *IEICE Trans. Electron.* E86-C, 372 (2003).
6. T. Durkop, S. A. Getty, E. Cobas, and M. S. Fuhrer, "Extraordinary mobility in semiconducting carbon nanotubes," *Nano Lett.* 4, 35 (2004).
7. T. Durkop, B. M. Kim, and M. S. Fuhrer, "Properties and applications of high-mobility semiconducting nanotubes," *Jour. Phys.: Condens. Matt.* 16, R553 (2004).
8. R. Saito, M. S. Dresselhaus, and G. Dresselhaus, *Physical properties of carbon nanotubes* (Imperial College Press, London, 1998).
9. Ph. Avouris, "Molecular electronics with carbon nanotubes," *Acc. Chem. Res.* 35, 1026 (2002).
10. H. C. d' Honincthun, S. G.-Retailleau, J. See, and P. Dollfus, "Electron-phonon scattering and ballistic behavior in semiconducting carbon nanotubes," *Appl. Phys. Lett.* 87, 172112 (2005).
11. R. Martel, V. Derycke, J. Appenzeller, S. Wind, and Ph. Avouris, "Carbon nanotube field-effect transistors and logic circuits," *IEEE Design Auto. Conf.*, 94 (2002).
12. S. J. Tans, A. R. M. Verschueuren, and C. Dekker, "Room temperature transistor based on a single carbon nanotube," *Nature* 393, 49 (1998).
13. S. J. Wind, J. Appenzeller, R. Martel, V. Derycke, and Ph. Avouris, "Vertical scaling of carbon nanotube field-effect transistors using top gate electrodes," *Appl. Phys. Lett.* 80(20), 3817 (2002).
14. Akturk, G. Pennington, and N. Goldsman, "Numerical performance analysis of carbon nanotube (cnt) embedded mosfets," *Proceeding of SISPAD*, 153 (2004).